GEOPHYSICS, VOL. 71, NO. 5 (SEPTEMBER-OCTOBER 2006); P. O33–O41, 12 FIGS.
10.1190/1.2231108

Fractured reservoirs: An analysis of coupled elastodynamic and permeability changes from pore-pressure variation

T. M. Daley[1], M. A. Schoenberg[1], J. Rutqvist[1], and K. T. Nihei[2]

ABSTRACT

Equivalent-medium theories can describe the elastic compliance and fluid-permeability tensors of a layer containing closely spaced parallel fractures embedded in an isotropic background. We propose a relationship between effective stress (background or lithostatic stress minus pore pressure) and both permeability and elastic constants. This relationship uses an exponential-decay function that captures the expected asymptotic behavior, i.e., low effective stress gives high elastic compliance and high fluid permeability, while high effective stress gives low elastic compliance and low fluid permeability. The exponential-decay constants are estimated for physically realistic conditions. With relationships coupling pore pressure to permeability and elastic constants, we are able to couple hydromechanical and elastodynamic modeling codes. A specific coupled simulation is demonstrated where fluid injection in a fractured reservoir causes spatially and temporally varying changes in pore pressure, permeability, and elastic constants. These elastic constants are used in a 3D finite-difference code to demonstrate time-lapse seismic monitoring with different acquisition geometries. Changes in amplitude and traveltime are seen in surface seismic P-to-S reflections as a function of offset and azimuth, as well as in vertical seismic profile P-to-S reflections and in crosswell converted S-waves. These observed changes in the seismic response demonstrate seismic monitoring of fluid injection in the fractured reservoir.

INTRODUCTION

The relationship between subsurface fluid-flow properties (e.g., permeability) and subsurface mechanical properties (e.g., elastic moduli, seismic velocities) is of increasing interest with the growth of time-lapse seismic surveys, which can be used to monitor reservoirs with changing fluid conditions. Typically, these surveys attempt to spatially locate changes in seismic properties, which can be used to infer changes in fluid properties (Greaves and Fulp, 1987; Rickett and Lumley, 2001; Swanston et al., 2003). Ideally, the changes in fluid properties and elastodynamic properties would be linked via constitutive relationships. The work of Biot (1956a,b) develops constitutive stress-strain and fluid-flow relationships in porous elastic media. For fractured media, theoretical studies investigate the effects of cracks and fractures on seismic wave propagation (O'Connell and Budiansky, 1976; Hudson, 1981). Work describing fractures as a displacement discontinuity has led to the use of an elastic compliance tensor (analogous to the permeability tensor) to describe the elastic moduli (Schoenberg, 1980; Schoenberg and Sayers, 1995). The effect of stress on both fluid flow and elastic properties has received much attention. A study by Shapiro (2003) analyzes the effect of stress dependence of compliant porosity on seismic velocity. Both the elastodynamic and flow properties of porous rock can be strongly dependent on the effective static stress. The effective stress, as a first approximation, is taken to be the differential stress, i.e., the external stress, often anisotropic, acting on a volume of rock, less the isotropic pore pressure (for positive stress defined as compression). Thus, for constant external stress, variation in effective stress is caused by variation in pore pressure. Furthermore, changes in pore pressure can affect the elastic compliance and permeability.

The elastic compliance can be considered to be made up of two parts: the compliance of the solid grains acting as if they are welded together and the compliance of the nonrigid grain boundaries and imperfections, such as microcracks and fractures. It is believed that the dependence of rock properties on effective stress is via the second part and that the compliance of the solid grains is relatively insensitive to changes in static stress. If we assume that rock imperfections are equivalent to one or more sets of aligned fractures and that the unfractured background is a consolidated rock of moderate po-

Manuscript received by the Editor April 23, 2004; revised manuscript received December 20, 2005; published online August 28, 2006.
[1]Lawrence Berkeley National Laboratory, Earth Sciences Division, 1 Cyclotron Rd., M.S. 90-1116, Berkeley, California 94720. E-mail: tmdaley@lbl.gov; maschoenberg@lbl.gov; jrutqvist@lbl.gov.
[2]Formerly Lawrence Berkeley National Laboratory, Berkeley, California. Presently Chevron ETC, 6001 Bollinger Canyon Rd., San Ramon, California 94583. E-mail: knih@chevron.com.

rosity (therefore relatively insensitive to changes in effective stress), then only those parts of the elastodynamic compliance tensor and the permeability tensor associated with the aligned fractures will depend on effective stress. This stress dependence of fracture compliance and permeability becomes a powerful way to look at the properties of fractured rock since, in this case, the dependence of rock properties on stress has a certain constrained form. This constrained form is the key assumption behind our subsequent analysis. In basic terms, this paper discusses seismic monitoring of fractured reservoirs.

We start by presenting a canonical problem representative of fractured reservoirs and use this problem to review equivalent-medium theories for fractured rocks and to introduce our constitutive relationship between pore pressure and both elastic properties and permeability. We then outline our coupled numerical modeling approach and give a specific example of coupled modeling. Finally, we present results of the hydromechanical and elastodynamic modeling.

A CANONICAL PROBLEM — MATERIAL PROPERTIES

We now study a three-layer problem with a fractured center layer and describe the elastic stiffness matrix, the permeability matrix, and the pore-pressure constitutive relationships.

Elastic stiffness matrix

Consider a vertically fractured layer sandwiched between a homogeneous, relatively impermeable, unfractured layer and a half-space of the same impermeable medium below. For simplicity, assume the fractures in the layer are axisymmetric about the fracture normal, closely spaced relative to a wavelength, and predominantly aligned in a single direction. Let the normal to those fractures be the x_1-direction and the strike be the x_2-direction (where x_1, x_2, $x_3 = x,y,z$).

For closely spaced (relative to a wavelength) parallel fractures, equivalent medium theories are a powerful way to obtain the elastodynamic compliance tensor and permeability tensor of the fractured rock. For compliance with the very small normal stress associated with seismic waves (slightly more or less compressive than the usual static compression), consider how much the fractures within a unit width of a rock will compress or dilate. Normal compression in the fractures per unit width is assumed to be linearly related to the (very small) excess normal stress, with the proportionality constant given by Z_N. Similarly, for axisymmetric fractures, the tangential motion in the fractures per unit width is assumed to be linearly related to, and aligned with, the (very small) excess tangential stress, with the proportionality constant given by Z_T. This formulation gives rise to a fracture compliance matrix $\mathbf{S}_f$ for axisymmetric fractures:

$$\mathbf{S}_f = \begin{bmatrix} Z_N & 0 & 0 \\ 0 & Z_T & 0 \\ 0 & 0 & Z_T \end{bmatrix},$$

which relates motion in the fractures per unit width to effective stress traction acting on the fracture plane (Schoenberg and Sayers, 1995). How these fracture compliances depend on effective stress is discussed below.

Equivalent-medium theories for fractured rocks (Schoenberg and Muir, 1989) and for this case of axisymmetric fractures (Schoenberg and Sayers, 1995) say that the fracture compliance matrix, when put into 6×6 contracted Voigt notation (Mavko et al., 1998), must be added to the compliance matrix of the unfractured background to give the overall elastodynamic compliance matrix of the fractured rock. This may be written explicitly in a simple form:

$$\mathbf{S} = \mathbf{S}_b + \mathbf{S}_f = \mathbf{S}_b + \begin{bmatrix} Z_N & 0 & 0 & 0 & 0 & 0 \\ 0 & 0 & 0 & 0 & 0 & 0 \\ 0 & 0 & 0 & 0 & 0 & 0 \\ 0 & 0 & 0 & 0 & 0 & 0 \\ 0 & 0 & 0 & 0 & Z_T & 0 \\ 0 & 0 & 0 & 0 & 0 & Z_T \end{bmatrix},$$

where $\mathbf{S}_b$ is the compliance matrix of the unfractured background, however anisotropic it may be, $\mathbf{S}_f$ is the compliance matrix of the fractures, and $\mathbf{S}$ is the total compliance matrix of the fractured rock. For an isotropic background with shear modulus μ_b and Poisson's ratio ν_b, Young's modulus E_b is given by

$$E_b = 2(1 + \nu_b)\mu_b = \frac{(1 - 2\nu_b)(1 + \nu_b)}{(1 - \nu_b)}(\lambda_b + 2\mu_b),$$

where λ_b is the second Lamé parameter. For this isotropic background, the elastodynamic compliance matrix is given by

$$\mathbf{S} = \mathbf{S}_b + \mathbf{S}_f = \begin{bmatrix} \frac{1}{E_b} + Z_N & \frac{-\nu_b}{E_b} & \frac{-\nu_b}{E_b} & 0 & 0 & 0 \\ \frac{-\nu_b}{E_b} & \frac{1}{E_b} & \frac{-\nu_b}{E_b} & 0 & 0 & 0 \\ \frac{-\nu_b}{E_b} & \frac{-\nu_b}{E_b} & \frac{1}{E_b} & 0 & 0 & 0 \\ 0 & 0 & 0 & \frac{1}{\mu_b} & 0 & 0 \\ 0 & 0 & 0 & 0 & \frac{1}{\mu_b} + Z_T & 0 \\ 0 & 0 & 0 & 0 & 0 & \frac{1}{\mu_b} + Z_T \end{bmatrix}. \quad (1)$$

For our canonical problem, the layer is assumed anisotropic and homogeneous. The form of the anisotropy (transverse isotropy) remains the same even as the layer becomes inhomogeneous, with its symmetry axis in the horizontal x_1-direction. There are five compliances for this transversely isotropic medium that depend on four parameters: E_b, μ_b, Z_N, and Z_T (since ν_b can be written in terms of E_b and μ_b, as shown previously); hence, there are only four independent elastic parameters for this medium.

The stiffness matrix $\mathbf{C}$ is the inverse of the compliance matrix $\mathbf{S}$. It is straightforward to show (Schoenberg and Sayers, 1995) that

$$\mathbf{C} = (\lambda_b + 2\mu_b) \times \begin{bmatrix} 1-\delta_N & r_b(1-\delta_N) & r_b(1-\delta_N) & 0 & 0 & 0 \\ r_b(1-\delta_N) & 1-r_b^2\delta_N & r_b(1-r_b\delta_N) & 0 & 0 & 0 \\ r_b(1-\delta_N) & r_b(1-r_b\delta_N) & 1-r_b^2\delta_N & 0 & 0 & 0 \\ 0 & 0 & 0 & \gamma_b & 0 & 0 \\ 0 & 0 & 0 & 0 & \gamma_b(1-\delta_T) & 0 \\ 0 & 0 & 0 & 0 & 0 & \gamma_b(1-\delta_T) \end{bmatrix}, \quad (2)$$

where

$$\gamma_b = \frac{\mu_b}{\lambda_b + 2\mu_b} = \frac{(1/2) - \nu_b}{1 - \nu_b},$$

$$r_b = \frac{\lambda_b}{\lambda_b + 2\mu_b} = \frac{\nu_b}{1 - \nu_b} = 1 - 2\gamma_b,$$

with γ_b being the square of the ratio of shear speed to compressional speed in the unfractured isotropic background and

$$\delta_T \equiv \frac{\mu_b Z_T}{1 + \mu_b Z_T}, \quad \delta_N \equiv \frac{(\lambda_b + 2\mu_b) Z_N}{1 + (\lambda_b + 2\mu_b) Z_N}.$$

Each δ represents the ratio of the strain taken up by the fractures to the corresponding total strain in the fractured rock (sum of the fracture contribution and the contribution of the background). Hence, δ_T and δ_N convey significant physical meaning, and it is more meaningful for them to be specified than the underlying Z.

Permeability matrix

We follow the development of Schoenberg (1991) to obtain a combined permeability matrix **K** for fractured, permeable, layered media; **K** is the sum of the fracture permeability matrix $\mathbf{K}_f$ and the unfractured background permeability matrix $\mathbf{K}_b$. The axisymmetric fractures introduce an excess permeability per unit width in the x_2- and x_3-directions, given by K_T, but no excess permeability in the x_1-direction (normal to the fractures). We thus have the relation

$$\mathbf{K} = \mathbf{K}_b + \mathbf{K}_f = \mathbf{K}_b + \begin{bmatrix} 0 & 0 & 0 \\ 0 & K_T & 0 \\ 0 & 0 & K_T \end{bmatrix}.$$

Note that $\mathbf{K}_b$ can have arbitrary anisotropy; however, for an isotropic unfractured background with scalar permeability K_b in all directions, the background permeability matrix $\mathbf{K}_b = K_b\mathbf{I}$, where **I** is the identity matrix and

$$\mathbf{K} = \mathbf{K}_b + \mathbf{K}_f = \begin{bmatrix} K_b & 0 & 0 \\ 0 & K_b + K_T & 0 \\ 0 & 0 & K_b + K_T \end{bmatrix}. \quad (3)$$

Here, too, it is useful to think of fracture permeability being some multiple of background permeability.

Pore-pressure constitutive relationships

Given the elastic stiffness matrix and the permeability matrix, a relationship to effective stress and thus to pore pressure is needed. We approach this relationship through our fractured-layer model. We consider a vertical well through a layer; the well will extract or inject fluid for a finite length of time Δt over the entire layer thickness. This creates pore-pressure gradients within the layer. Under our assumptions, only the fracture permeability and the fracture compliance will change, both as functions of spatial location and time. Many unknowns are involved in such a process — in particular, how much a particular pore-pressure rise (or drop) will increase (or decrease) elastodynamic compliance and fluid permeability. However, because only the contributions of the fractures to these quantities are assumed to be significant, just three parameters must be estimated — the normal and tangential fracture compliance and fracture permeability. These three parameters are a function of the normal effective stress $\sigma_{11_{\text{eff}}}$. The background properties are held constant.

A reasonable approach is to assume very high values of fracture compliance and permeability at low normal effective stress. Then the fracture compliances and fracture permeability approach low values asymptotically as normal stress becomes large. We estimate such dependence by exponential decay functions suggested in laboratory studies by Bandis et al. (1983) and Barton et al. (1985). Thus, we propose that Z_N and Z_T are given by

$$\begin{aligned} Z_T &= Z_{T_\infty} + [Z_{T_0} - Z_{T_\infty}]e^{-\sigma_{11_{\text{eff}}}/\tau_T}, \\ Z_N &= Z_{N_\infty} + [Z_{N_0} - Z_{N_\infty}]e^{-\sigma_{11_{\text{eff}}}/\tau_N} \end{aligned} \quad (4)$$

and fracture permeability K_T is given by

$$K_T = K_{T_\infty} + [K_{T_0} - K_{T_\infty}]e^{-\sigma_{11_{\text{eff}}}/\tau_K}, \quad (5)$$

where τ_T, τ_N, and τ_K are decay constants for Z_T, Z_N, and K_T, respectively.

The values of τ specify the rate of exponential decrease of compliance or permeability with increasing effective stress. The subscript 0 indicates values for very low effective stress acting normal to the fractures; the subscript ∞ indicates values for very high effective stress acting normal to the fractures. With these nonlinear constitutive relations we can calculate the change in fracture compliance and permeability for a given change in pore pressure resulting from injection or withdrawal, leading to inhomogeneous compliance and permeability within the fractured layer. With the new inhomogeneous fracture compliance, the elastic moduli are calculated and the seismic response can be modeled.

After initial fluid injection or withdrawal for a time interval Δt, the new heterogeneous compliance and permeability are used as the fluid continues to be extracted or injected from the well for an additional time interval Δt, changing the pore pressure and yielding another set of values for permeability and elastic moduli.

COUPLED MODELING APPLICATION

In outline, building a specific coupled numerical model proceeds with the following steps.

1) For a given model geometry (spatial dimensions, number of layers, and their thicknesses), select the background material properties: α, β, ρ, ϕ, K, and p (P-wave velocity, S-wave velocity, density, porosity, permeability, and pore pressure, respectively).

2) Calculate the initial external stress σ_{ext} at reservoir depth using the density model and hydrostatic pressure assumption. We assume that density does not change with pressure.
3) Assign fracture properties at zero effective stress (δ_{T_0}, δ_{N_0}, and K_{T_0}) and at infinite effective stress (δ_{T_∞}, δ_{N_∞}, and K_{T_∞}).
4) Assign decay constants for stress dependence of compliance and permeability: τ_T, τ_N, τ_K.
5) Calculate the initial, homogeneous, anisotropic elastic constants in the reservoir using equations 2 and 4 and $\sigma_{11_{eff}} = \sigma_{ext} - p$. We assume that σ_{ext} is constant, an assumption that could be relaxed in future work. The initial homogeneous pore pressure is assumed as given. Note that this model assumes a thin reservoir with constant properties. For thicker reservoirs σ_{ext} would vary with depth, and the elastic constants C_{ij} might not be homogeneous with depth.
6) For the initial seismic response, perform preinjection seismic modeling.
7) Perform the initial fluid injection hydromechanical modeling with a given injection rate. Calculate the new pore pressure at each spatial location using initial homogeneous anisotropic permeability (equation 3).
8) At each time step of the hydromechanical modeling, calculate p, $\sigma_{11_{eff}}$, Z_N, Z_T, and K_T and update **S** and **K** for each spatial location.
9) At selected time intervals, perform seismic modeling with updated elastic constants (which are now heterogeneous through the spatially dependent Z_N and Z_T).
10) Repeat steps 8 and 9 for the desired intervals.

A specific simulation

Following the outline above, we designed our simulation beginning with background properties and geometry. The model has three layers: a 500-m surface layer, a 60-m fractured layer, and a half-space below. For simplicity, the top layer and bottom half-space are relatively impermeable, homogeneous, and isotropic, with compressional-wave speed α, and shear-wave speed β (km/s), and specific density ρ (g/cm^3) given by $\alpha = 3.8$, $\beta = 2.2$, and $\rho = 2.4$.

The vertically fractured layer has an in-situ external stress of $2.4 \times 5 = 12$ MPa, where 2.4 is obtained from an assumed average specific gravity of formation above the layer and 5 MPa is obtained from 10 atm $\sim$ 1 MPa per 100 m water depth. We assume static and dynamic properties are the same (a rigorously unjustified but simplifying assumption). We have chosen as background parameters $\alpha_b = 4.550$ km/s, $\beta_b = 2.432$ km/s, $\rho_b = 2.40$ g/cm^3, background porosity $\phi_b = 0.15$, and permeability $K_b = 0.1$ darcy. These quantities correspond to $\nu_b = 0.300$, $\gamma_b = 0.2857$, and $r_b = 0.4286$ and elastic moduli of $\lambda_b + 2\mu_b = 49.686$ GPa, $\lambda_b = 21.2958$ GPa, $\mu_b = 14.1951$ GPa, and $E_b = 36.9073$ GPa. The fracture compliances are picked from considerations of the values of δ at zero effective stress:

$$\delta_{T_0} \equiv \frac{\mu_b Z_{T_0}}{1 + \mu_b Z_{T_0}} = 0.6 \quad \text{or} \quad \mu_b Z_{T_0} = 1.5$$

and

$$\delta_{N_0} \equiv \frac{(\lambda_b + 2\mu_b) Z_{N_0}}{1 + (\lambda_b + 2\mu_b) Z_{N_0}} = 0.2 \quad \text{or}$$

$$(\lambda_b + 2\mu_b) Z_{N_0} = 0.25.$$

This gives $Z_{T_0} = 0.1057$ GPa^{-1} and $Z_{N_0} = 5.032 \times 10^{-3}$ GPa^{-1}.

We let $Z_{T_\infty} = Z_{T_0}/5$ and Z_T's decay rate with stress $\tau_T = 2$ MPa. Similarly, we let $Z_{N_\infty} = Z_{T_0}/2$ and Z_N's decay rate with stress $\tau_N = 2$ MPa. We also assume that $K_{T_0} = 50$ darcies, $K_{T_\infty} = K_{T_0}/100$, and K_T's decay rate with stress $\tau_K = 2$ MPa. Then we start at a pore pressure p of 2.5 MPa so the starting value of effective normal stress is $\sigma_{11_{eff}} = \sigma_{ext} - p$, which is 12 − 2.5 MPa = 9.5 MPa. We assume the external stress is isotropic; it is easy to relax this assumption and let the overburden stress be different from a rotationally symmetric horizontal external stress.

Using the above background properties, we can calculate the initial fracture compliance and permeability in the fractured layer. Using equation 4, we find the initial compliances are

$$Z_T = Z_{T_\infty} + [Z_{T_0} - Z_{T_\infty}]e^{-4.75} = Z_{T_0}\left[\frac{1 + 4e^{-4.75}}{5}\right] = 0.207 Z_{T_0}$$

and

$$Z_N = Z_{N_\infty} + [Z_{N_0} - Z_{N_\infty}]e^{-4.75} = Z_{N_0}\left[\frac{1 + e^{-4.75}}{2}\right] = 0.504 Z_{N_0}.$$

Similarly, from equation 5 we calculate fracture permeability to be

$$K_T = K_{T_\infty} + [K_{T_0} - K_{T_\infty}]e^{-4.75} = K_{T_0}\left[\frac{1 + 99e^{-4.75}}{100}\right] = 0.0186 K_{T_0}.$$

The values of δ at $t = 0$ are given by

$$\delta_T|_{t=0} = \frac{1.5 \times 0.207}{1 + 1.5 \times 0.207} = 0.2369,$$

$$\delta_N|_{t=0} = \frac{0.25 \times 0.504}{1 + 0.25 \times 0.504} = 0.1119.$$

Thus, the homogeneous medium at $t = 0$ (the time when the pore pressure is 2.5 MPa everywhere in the layer) has elastic constants C_{ij}, where

$$\mathbf{C} = \begin{bmatrix} 44.126 & 18.913 & 18.913 & 0 & 0 & 0 \\ 18.913 & 48.665 & 20.274 & 0 & 0 & 0 \\ 18.913 & 20.274 & 48.665 & 0 & 0 & 0 \\ 0 & 0 & 0 & 14.195 & 0 & 0 \\ 0 & 0 & 0 & 0 & 10.832 & 0 \\ 0 & 0 & 0 & 0 & 0 & 10.832 \end{bmatrix} \text{GPa}. \quad (6)$$

The model is now specified and ready for initial hydromechanical and seismic calculations.

HYDROMECHANICAL MODELING

Hydromechanical modeling calculates the evolution of a fractured reservoir's elastic compliance and permeability during fluid injection. The resulting changes in elastic compliance (including normal and shear components) are then used as input to the elastodynamic (seismic) modeling code.

Hydromechanical model setup

Since the fractured layer is assumed to contain one set of fractures, which are oriented vertically and have permeability much larger than the surrounding unfractured rock, the hydromechanical injection simulation is numerically simplified by using a 2D one-layer model located at the center plane of the fractured reservoir (Figure 1). From a hydraulic point of view, the model's reservoir layer is confined between impermeable boundaries of vertical symmetry planes and horizontal interfaces with impermeable material above and below. The model is one-quarter symmetric, measuring 4 × 4 km in the horizontal plane. At the far boundaries (4 km away from the injection point) the fluid pressure is assumed to be constant.

The mechanical boundary conditions allow no displacements normal to the vertical symmetry planes and fix a constant horizontal stress of 12 MPa acting normal to the far boundaries. The bottom surface of the model has fixed vertical displacement. A constant vertical stress of 12 MPa (lithostatic stress) is imposed on the top of the reservoir layer. A constant vertical stress on the top of the reservoir layer is more realistic than a no-displacement condition because the ground surface, located 500 m above, is free to move.

Using the background material properties and equations 4 and 5, the variation of compliance and permeability with effective normal stress is shown in Figures 2 and 3. The permeability gives a reasonable rate of fluid propagation along the fracture direction during injection. This results in a background permeability of 0.1 darcy and an initial fracture permeability along the direction of the fractures of 0.9 darcy. These values are within the range of fractured rocks [see Table 2.2 in Freéze and Cherry (1979)]. In addition, we assume Biot's $\alpha = 1$ (incompressive grains); Biot's modulus M is estimated as $1/(\phi C_W) = 22.7$ GPa (assuming incompressible grains) for $\phi = 0.1$, and the compressibility of water $C_W = 4.4 \times 10^{-10}$ Pa^{-1} (Biot, 1941; Noorishad et al., 1982). The exact value of M has little impact on the evolution of fluid pressure during injection because aquifer storage of water is dominated by the pressure-induced mechanical opening of fractures. The value of Biot's α could be smaller than unity, with the main effect being that the effective stress would change less for a given fluid pressure change and hence the hydromechanical responses would be less pronounced.

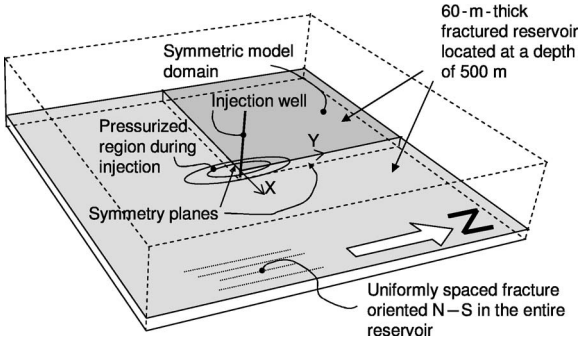

Figure 1. Specific simulation geometry and quarter-symmetric model domain for hydromechanical simulation.

Hydromechanical simulation results

The injection simulation was conducted with the finite-element ROCMAS program (Noorishad et al., 1982; Noorishad and Tsang, 1996), giving a fully coupled hydromechanical analysis. Injection is conducted at a constant rate of 80 litres/minute for the entire 60-m-thick layer. Figure 4 presents the injection pressure versus time for simulations with and without consideration of hydromechanical changes. The lower injection pressure for the hydromechanical case is mainly a result of the increased fracture permeability as fractures are forced open by internal fluid pressure. According to Figure 3, the fracture permeability can increase by more than one order of magnitude when the increasing fluid pressure reduces the effective normal stress toward zero. This prevents the fluid pressure from exceeding the total (external) stress normal to fractures. Therefore, in the hydromechanical case the fluid pressure stays just below total (external) stress normal to fractures (about 12 MPa).

Figure 5 presents the distribution of fluid pressure and effective stress normal to the fracture planes after two months of injection. As expected, the fluid pressure distribution is anisotropic, with a more rapid propagation of fluid pressure along the fracture strike (*y*-

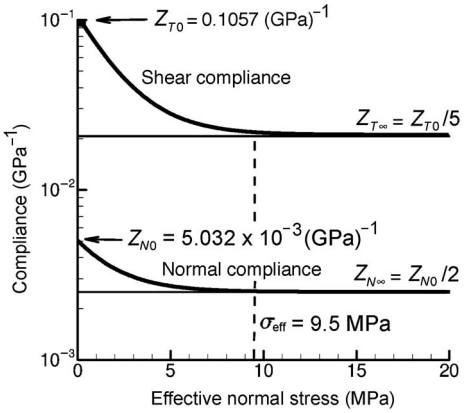

Figure 2. Relationship between effective stress and shear compliance (top) and effective stress and normal compliance (bottom).

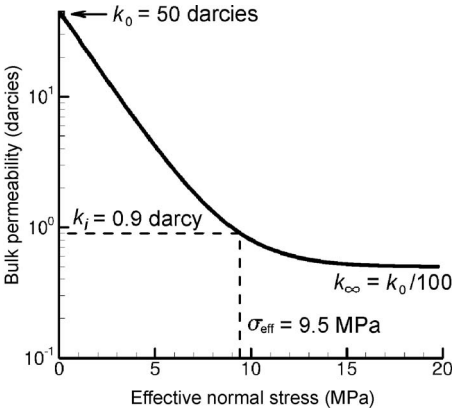

Figure 3. Permeability as a function of effective stress for the parameters used in modeling.

direction in Figure 5). At two months, a pressure increase of more than 0.5 MPa has propagated as far as 3.3 km along the fractures. In fact, at two months, the pressure distribution along the fracture strike has almost reached steady state and is controlled by the constant-pressure boundary conditions at 4 km. Figure 5b shows that the largest reduction in effective normal stress occurs near the injection well, where high fluid pressure results in an effective normal stress close to zero.

Figure 6 presents the distribution of changes in shear and normal compliance after two months of injection. The largest changes of fracture compliance occur near the injection well in a zone of low effective stress extending along the strike of the fractures. The maximum changes in shear and normal compliances in Figure 6 are limited by the assumed ratios of $Z_{T_0}/Z_{T_\infty} = 5$ and $Z_{N_0}/Z_{N_\infty} = 2$, as shown in Figure 2. These assumed ratios might be conservative, and higher ratios would result in larger changes. The simulation result at two months, with a heterogeneous distribution of normal and shear compliances, was converted to three dimensions by assuming a constant vertical distribution within the thin reservoir layer and a symmetrical distribution of compliances from the modeled quadrant (0°–90° azimuth) around the injection borehole (see Figure 1).

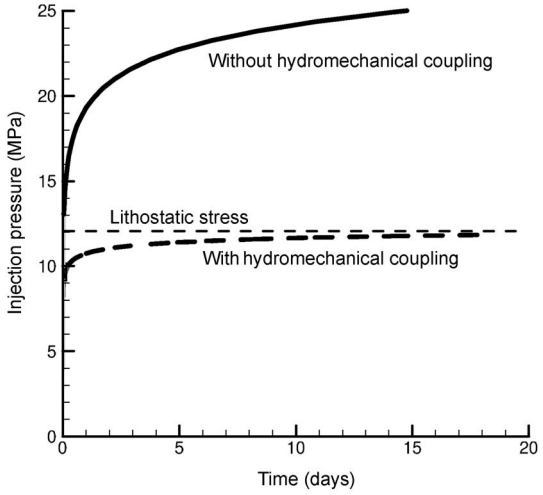

Figure 4. Injection pressure as a function of time with and without consideration of hydromechanical coupling.

THREE-DIMENSIONAL ANISOTROPIC SEISMIC MODELING

At specific times in the hydromechanical modeling, the spatially heterogeneous fracture compliances were used to calculate elastic constants. Two time steps are discussed: the initial preinjection model (homogeneous anisotropic) and the two-month postinjection model (heterogeneous anisotropic). The variable grid blocks used in finite-element hydromechanical modeling were interpolated linearly to an equally spaced grid for finite-difference modeling. Furthermore, the 2D hydromechanical model of the reservoir was expanded to three dimensions using the symmetry properties described above.

The seismic 3D finite-difference code is a fourth order staggered-grid implementation (Levander, 1988; Nihei et al., 1999) that models fractures using the method of equivalent media. Three components of velocity plus pressure and stresses can be output for each sensor. We could have inserted discrete fractures using the method of Coates and Schoenberg (1995), but these would introduce too much internal scattering (Nakagawa et al., 2003, 2004). The finite-difference model measured 291 × 291 × 218 grid points (x,y,z), including a 20 grid-point absorbing boundary on all sides. The spatial grid size was 6 m; the total model was thus 1746 × 1746 × 1308 m (x,y,z), including the 120-m absorbing boundary on all sides. For an explosive-type source with a 30-Hz Ricker wavelet, the calculated time step was 0.5 ms. One second of data (2000 time steps) was calculated. As an example of potential seismic monitoring schemes,

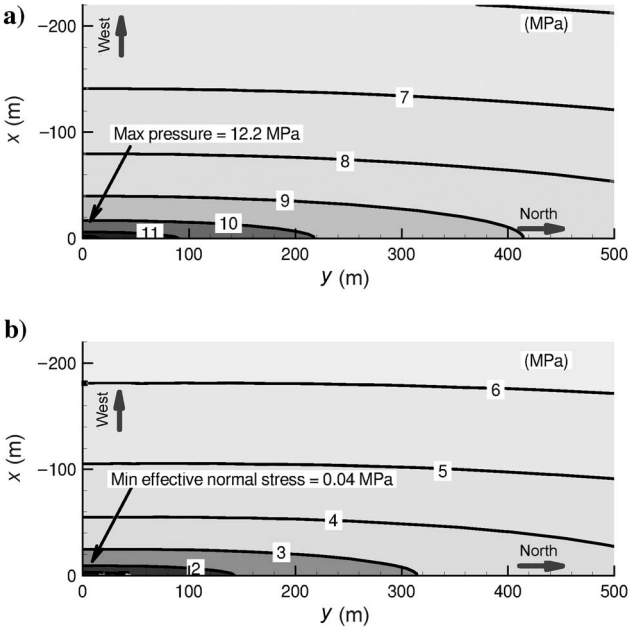

Figure 5. Plan view showing distribution of fluid pressure (a) and effective normal stress across fractures (b) after two months of injection (see Figure 1 for location of x- and y-axes).

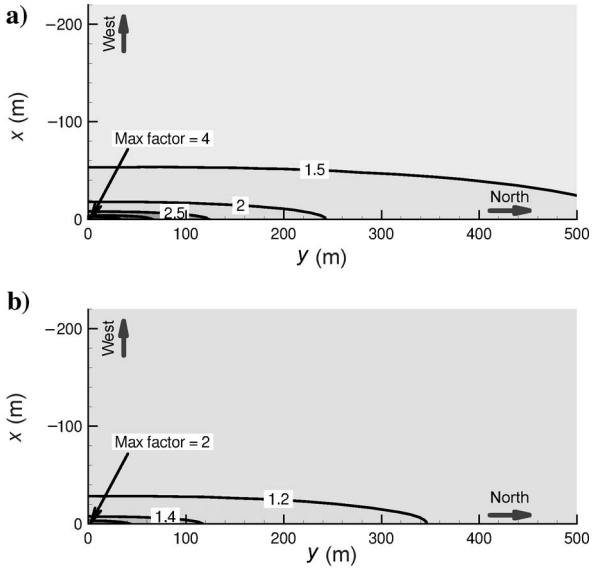

Figure 6. Plan view showing change factor for shear compliance (a) and normal compliance (b) relative to initial (preinjection) values (see Figure 1 for location of x- and y-axes).

shot gathers were calculated for three different acquisition geometries: surface seismic, vertical seismic profile (VSP), and horizontal-well crosswell (shown schematically in Figure 7).

Surface seismic model

The 3D surface seismic shot gather had sensors at 24 m spacing in both *x*- (east-west) and *y*- (north-south) directions, giving 57 sensors on each of 57 receiver lines (which were 1344 m long) for a total of 3249 surface sensors (Figure 7a). While the 3D finite-difference code calculates three components of motion, only the vertical component is analyzed here, as vertical geophones are the predominant field survey sensor in use today. The source point was slightly offset (17 m at 45° azimuth) from the injection well. Figure 8 shows the vertical-component gathers for each 90° of azimuth and for a time window which includes the P-to-P reflection (250–350 ms) and the P-to-S converted reflection (350–450 ms).

Analysis of the results shows very small time-lapse changes in amplitude or traveltime of the P-to-P reflection; such changes probably would be undetectable in field data with noise. However, there is an observable change in the P-to-S reflection. Variation in amplitude with azimuth, most evident in the P-to-S reflection in Figure 8, is present in the data generated using the initial homogeneous anisotropic model and in the postinjection, heterogeneous anisotropic model. The time-lapse change in peak amplitude of the P-to-S reservoir reflection, as a function of azimuth and offset, is shown in Figure 9. For near offsets (less than 200 m), the small P-to-S reflection amplitude caused scatter in the ratio; these data are not shown. At offsets greater than 200 m, the azimuths parallel to the fractures, 180° and 0° (360°), have no significant time-lapse amplitude change, while the azimuths normal to fractures, 90° and 270°, have about 5%–30% change, decreasing with offset.

The negative time-lapse amplitude change observed in the shot gather is explained by the increased fracture compliance for fracture-normal propagation within the reservoir, which decreases the velocity of the high-velocity reservoir layer and thus decreases the reflection coefficient. The difference between the 90° and 270° time-lapse changes is presumably from the small offset of the source to the east (90°), which means the 270° reflection points have greater change in compliance for the equivalent offset distance. The variation with offset and azimuth shown in Figure 9 does not originate from a single reflection point because the data are a shot gather, not a common-midpoint (CMP) gather. The heterogeneous anisotropy of the postinjection model causes each source-receiver reflection point to have different properties. Full CMP analysis would require calculation and analysis of a complete numerical 3D surface seismic data set — a task beyond the scope of this paper.

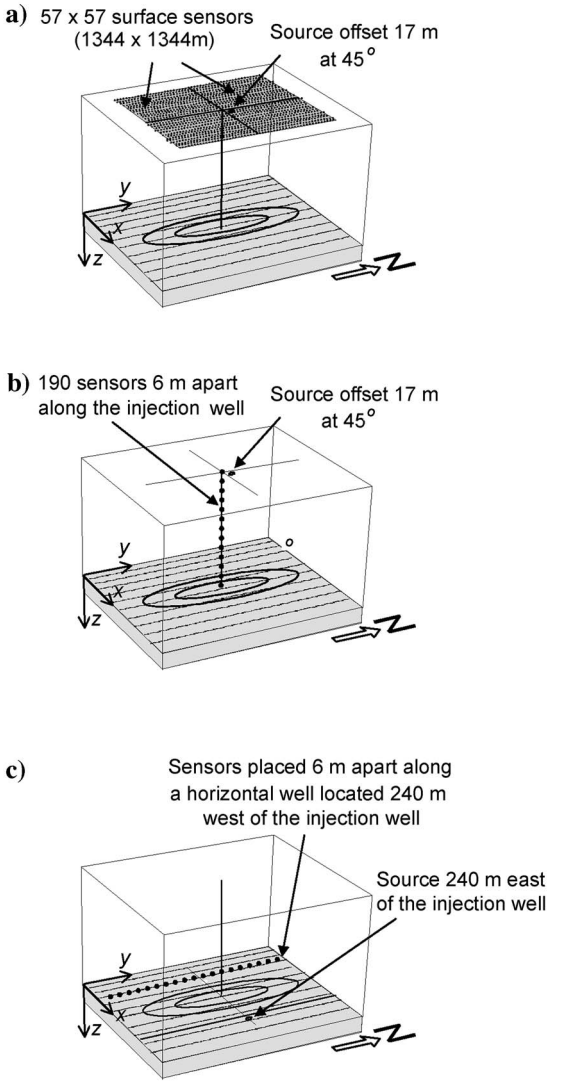

Figure 7. Acquisition geometries for 3D seismic finite-difference modeling. Shot gathers were calculated for (a) surface seismic, (b) VSP, and (c) horizontal crosswell models.

Vertical seismic profile model

A common method for seismic detection of fractured reservoirs is the VSP. We used the 3D seismic model to generate a three-component (3-C) receiver, single-source VSP data set. The sensors were located at the injection well with 6 m spacing, giving 190 total sensors

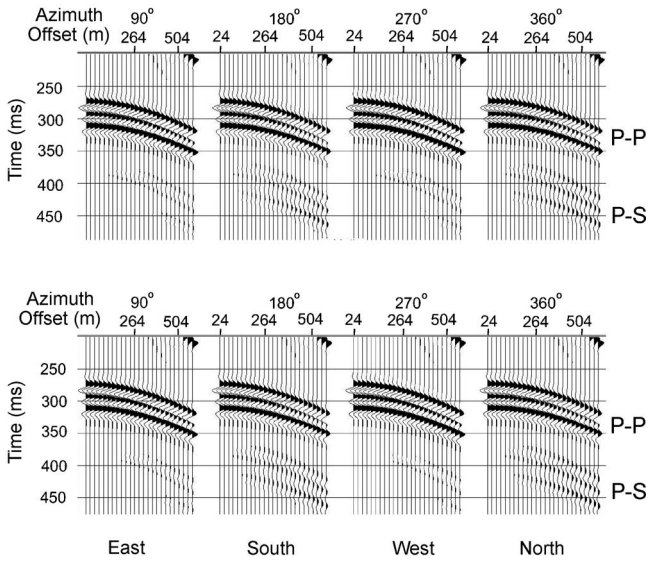

Figure 8. Azimuth gathers of vertical-component shot gather for the P-to-P and P-to-S reservoir layer reflections for preinjection (top) and postinjection (bottom) data. Direct arrival is seen at early time and large offset (upper right of each plot).

(Figure 7b). The source was the same as for the surface seismic survey, 17 m from the borehole at 45° azimuth. Data were calculated for the preinjection model and the two-month postinjection model. With VSP surveys, it is common to record 3-C data; therefore, we analyze the horizontal component to enhance our observations of the P-to-S conversion. Figure 10 shows the horizontal component of velocity V_x calculated for sensors in the injection borehole. A time-lapse amplitude change in the P-to-S reflection is observable, especially for the later-arriving reservoir-bottom reflection, which is also delayed by increased fracture compliance in the postinjection reservoir layer.

Horizontal crosswell model

Crosswell seismic surveying in horizontal wells is an emerging technology. Horizontal wells can increase fluid production from vertically fractured reservoirs because of the greater number of fractures intersected. Horizontal crosswell geometry allows more spatial sampling from waves propagating within a layer. We modeled a crosswell shot gather for a borehole parallel to the fracture strike and within the reservoir layer (Figure 7c). While many horizontal wells are drilled normal to the expected fracture-strike direction, at least one modern horizontal-well development (Weyburn field in Canada) is drilled parallel to the expected fracture strike to improve matrix fluid recovery. In our model, the sensor well was 240 m west of the injection well, with sensors every 6 m, and the source was 240 m east of the injection well. Note that the single source modeled here could be located in either a vertical or a horizontal well.

Figure 11 shows a shot gather for the preinjection and two-month postinjection models using V_x. A change in the P-to-S converted wave amplitude and traveltime is seen between 280 and 300 ms for near-zero offsets. This time-lapse change is from the changing compliance of the fractured reservoir during injection. The change in S-wave velocity is apparent on time snapshots of the wavefield. Figure 12 shows wavefield snapshots of the x-component of particle velocity in the vertical y-z plane. A slowing of the S-wave in the reservoir layer after injection is apparent in the wavefield snapshot.

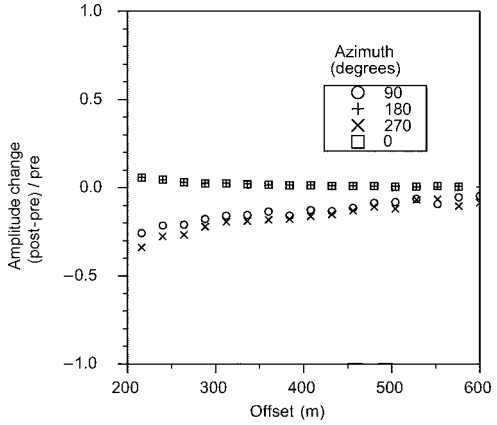

Figure 9. Time-lapse change in peak amplitude of P-to-S reflection from the fractured layer for select azimuths as a function of source-receiver offset. The change is normalized to the preinjection amplitude. Note that 90° and 270° are normal to fractures and 180° and 360° are parallel to fractures. Azimuth is measured clockwise from due north.

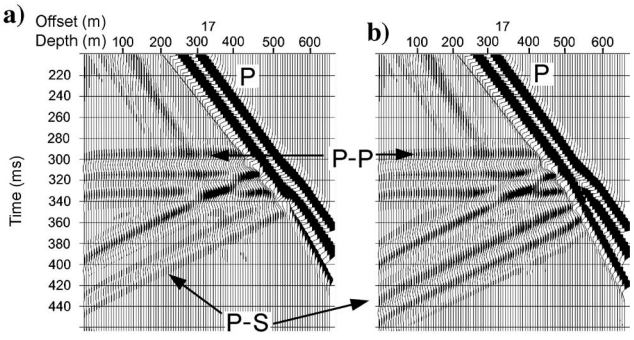

Figure 10. The x-component VSP data for (a) preinjection and (b) postinjection models. Data are time shifted to two-way P-wave time, causing the P-to-P reservoir reflection to be aligned at about 300 ms. Labeled offset is the horizontal source offset from the well location. The most observable change is in the P-to-S converted reflection from the bottom of the reservoir layer (labeled P-S).

DISCUSSION

In future work, additional fracture sets could be included, distributions of fracture orientation could be considered, or the equivalent medium model could be dropped in favor of discrete fractures. In addition, the restriction that background properties are independent of

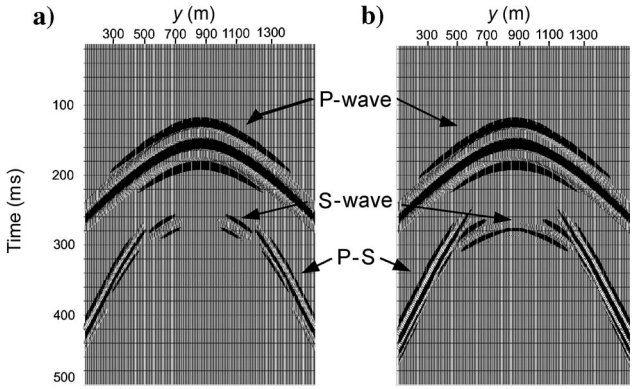

Figure 11. Crosswell shot gather for horizontal wells within the reservoir layer for (a) preinjection and (b) postinjection models. The sensors are spaced every 6 m in the y-direction. The source y-coordinate is 876 m.

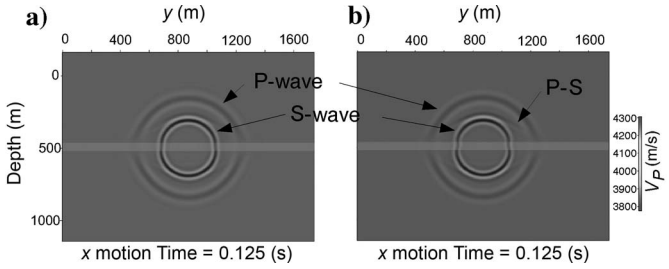

Figure 12. Wavefield snapshot showing the x-component of velocity at 0.125 s in the y-z plane (which contains the injection well) for (a) the preinjection model and (b) the postinjection model. The P-wave velocity model is superimposed. The source is in the reservoir layer 240 m away for this model of crosswell propagation.

effective stress could be relaxed. More extensive modeling could include complete 3D seismic surveys which would allow spatial imaging of the reservoir property changes.

Another important extension to consider is monitoring with controlled shear-wave sources, allowing optimal measurement of shear-wave splitting. Monitoring vertical fracture properties may be best accomplished using shear-wave sources and 3-C sensors with small receiver offsets (although this is difficult in some locations such as offshore). Monitoring unconverted shear waves, with a goal of measuring shear-wave splitting, would be similar to measuring the fracture shear compliance as defined by linear slip deformation theory. Because this type of shear-wave monitoring is often unfeasible, we offer our numerical simulation as a method to explore some ways that time-lapse information from compressional waves and converted shear waves can be acquired and analyzed.

Many refinements and parameters could be included in coupled modeling to help us understand the nature of time-lapse changes of fractured reservoir properties. Different approaches to this problem can be taken. Our approach is a framework on which to hang different features and approaches to a fractured-reservoir study. Such features and approaches include anisotropic attenuation, multiple scattering, discrete fractures, and modeling fractures as a collection of very oblate ellipsoidal or penny-shaped cracks. Other possible relationships between effective stress and fluid permeability/elastic compliance can be investigated using this framework. Comparison and calibration of models with laboratory and field-scale experiments will test these approaches.

SUMMARY

For closely spaced parallel fractures embedded in an isotropic background medium, equivalent-medium theories describe the elastic constants and fluid permeability. When fluid is injected or withdrawn from a reservoir, the pore pressure and effective stress change spatially and temporally. To model these changes, a relationship between effective stress and both permeability and elastic constants must be specified. We propose an exponential decay function that captures the asymptotic relationships between effective stress and permeability/compliance, i.e., low normal effective stress (external stress minus pore pressure) gives high elastic compliance and fluid permeability while high normal effective stress gives low elastic compliance and fluid permeability. A decay constant was estimated for physically realistic conditions. Having related pore pressure to permeability and elastic compliance, we were able to couple hydromechanical and elastic-wave modeling algorithms. The coupled codes were used to model the spatial and temporal changes in fracture permeability and elastic compliance within a fractured reservoir that arise from fluid injection in a single well. The effective stress decreased and fracture compliance increased predominantly along fracture strike, as expected. Various seismic acquisition geometries were modeled to show the applicability of time-lapse monitoring of fluid injection or withdrawal. For the relatively modest decay constants used in our model, borehole seismic geometry (VSP or crosswell) most easily detected the time-lapse change. For a point source, the P-to-S converted wave showed the most easily observed changes. The observed changes in a surface seismic shot gather implies that modeling and processing of a complete 3D surface seismic survey should allow spatial mapping of the change in fracture properties.

ACKNOWLEDGMENTS

This work was supported by the Assistant Secretary for Fossil Energy, National Petroleum Office of the U.S. Department of Energy, and by the Director, Office of Science, Office of Basic Energy Sciences, Division of Chemical Sciences, Geosciences and Biological Sciences of the U.S. Department of Energy, under contract DE-AC03-76-SF00098. Seismic computations were performed at the Center for Computational Seismology, supported by the Office of Basic Energy Sciences. Thanks go to the reviewers for helpful suggestions and to John Queen for help with the seismic finite-difference code and general discussions.

REFERENCES

Bandis, S. C., A. C. Lumsden, and N. R. Barton, 1983, Fundamentals of rock joint deformation: International Journal of Rock Mechanics, Mining Science and Geomechanics Abstracts, **20**, 249–268.

Barton, N., S. Bandis, and K. Bakhtar, 1985, Strength, deformation and conductivity coupling of rock joints: International Journal of Rock Mechanics, Mining Science and Geomechanics Abstracts, **22**, 121–140.

Biot, M. A., 1941, General theory of three-dimensional consolidation: Journal of Applied Physics, **12**, 155–164.

———, 1956a, Theory of propagation of elastic waves in a fluid saturated porous solid. I. Low frequency range: Journal of the Acoustical Society of America, **28**, 168–178.

———, 1956b, Theory of propagation of elastic waves in a fluid saturated porous solid. II. Higher-frequency range: Journal of the Acoustical Society of America, **28**, 179–191.

Coates, R. T., and M. Schoenberg, 1995, Finite-difference modeling of faults and fractures: Geophysics, **60**, 1514–1526.

Freéze, A. R., and J. A. Cherry, 1979, Groundwater: Prentice-Hall Inc.

Greaves, R. J., and T. J. Fulp, 1987, Three-dimensional seismic monitoring of an enhanced oil recovery process: Geophysics, **52**, 1175–1187.

Hudson, J., 1981, Wave speeds and attenuation of elastic waves in material containing cracks: Geophysical Journal of the Royal Astronomical Society, **64**, 133–150.

Levander, A. R., 1988, Fourth-order finite-difference P-SV seismograms: Geophysics, **53**, 1425–1436.

Mavko, G., T. Mukerji, and J. Dvorkin, 1998, The rock physics handbook: Cambridge University Press.

Nakagawa, S., K. T. Nihei, and L. R. Myer, 2003, 3-D elastic wave scattering by a layer containing vertical periodic fractures: Journal of the Acoustical Society of America, **113**, 3012–3023.

———, 2004, Plane wave solution for elastic wave scattering by a heterogeneous fracture: Journal of the Acoustical Society of America, **115**, 2761–2772.

Nihei, K. T., W. Yi, L. R. Myer, N. G. W. Cook, and M. Schoenberg, 1999, Fracture channel waves: Journal of Geophysical Research, **104**, 4769–4781.

Noorishad, J., M. S. Ayatollahi, and P. A. Witherspoon, 1982, A finite element method for coupled stress and fluid flow analysis of fractured rocks: International Journal of Rock Mechanics, Mining Science and Geomechanics Abstracts, **19**, 185–193.

Noorishad, J., and C. Tsang, 1996, ROCMAS-simulator: A thermohydromechanical computer code, *in* O. Stephansson, L. Jing, and C. Tsang, eds. Coupled thermo-hydromechanical processes of fractured media. Elsevier Scientific Publ. Co., 551–558.

O'Connell, R., and B. Budiansky, 1976, Seismic velocities in dry and saturated cracked solids: Journal of Geophysical Research, **79**, 5412–5426.

Rickett, J. E., and D. E. Lumley, 2001, Cross-equalization data processing for time-lapse seismic reservoir monitoring: A case study from the Gulf of Mexico: Geophysics, **66**, 1015–1025.

Schoenberg, M., 1980, Elastic wave behavior across linear slip interfaces: Journal of the Acoustical Society of America, **68**, 1516–1521.

———, 1991, Layered permeable systems: Geophysical Prospecting, **39**, 219–240.

Schoenberg, M., and F. Muir, 1989, A calculus for finely layered anisotropic media: Geophysics, **54**, 581–589.

Schoenberg, M., and C. M. Sayers, 1995, Seismic anisotropy of fractured rock: Geophysics, **60**, 204–211.

Shapiro, S. A., 2003, Elastic piezosensitivity of porous and fractured rocks: Geophysics, **68**, 482–486.

Swanston, A. M., P. B. Flemings, J. T. Comisky, and K. D. Best, 2003, Time-lapse imaging at Bullwinkle field, Green Canyon 65, offshore Gulf of Mexico: Geophysics, **68**, 1470–1484.